Supplementary Information

Giant Transition-State Quasiparticle Spin-Hall Effect in an Exchange-Spin-Split Superconductor Detected by Nonlocal Magnon Spin Transport

Kun-Rok Jeon,* Jae-Chun Jeon, Xilin Zhou, Andrea Migliorini,

Jiho Yoon and Stuart S. P. Parkin*

Max Planck Institute of Microstructure Physics, Weinberg 2, 06120 Halle (Saale), Germany

*To whom correspondence should be addressed: jeonkunrok@gmail.com, stuart.parkin@halle-mpi.mpg.de

This PDF file includes:

Supplementary Text

Figs. S1 to S6

References (*S1*-*S22*)

Section S1. Estimation of the magnon spin-diffusion length of YIG.

In this section, we estimate the magnon spin-diffusion length l_{sd}^{m} of 200-nm-thick single-crystalline YIG films used in the present study. According to the fabrication process outlined in Method, we prepare reference devices composed of Pt injector and detector only (Fig. S1a-d). These Pt are separated by a center-to-center distance d^{Pt-Pt} of 9−18 μm, which corresponds to the regime where magnon spin currents decay exponentially.[S1] One can thus estimate l_{sd}^{m} from the d^{Pt-Pt}-dependent non-local voltages (ΔV_{nl}^{el} and ΔV_{nl}^{th} in Fig. S1e-h) using simple formulas:

$$\Delta V_{nl}^{el} = A\exp\left(-\frac{d^{Pt-Pt}}{l_{sd}^{m}}\right), \qquad \text{(S1a)}$$

$$\Delta V_{nl}^{th} = B\exp\left(-\frac{d^{Pt-Pt}}{l_{sd}^{m}}\right), \qquad \text{(S1b)}$$

where A and B are the proportional factor that is irrelevant to d^{Pt-Pt}. By fitting Eq. (Sl) to the summarized data of $\Delta V_{nl}^{el}(d^{Pt-Pt})$ and $\Delta V_{nl}^{th}(d^{Pt-Pt})$ in Fig. S1i, we get l_{sd}^{m} = 11 and 9 μm for the electrically and thermally driven magnons, respectively, at room temperature. Both cases appear to be almost independent of T_{base} (Fig. S1j). These are in good agreement with previous experiments[S2,S3] based on YIG thin films of similar quality and thickness.

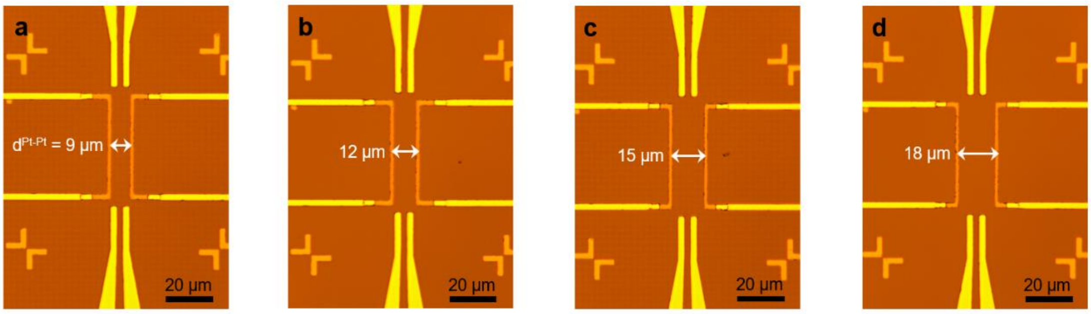

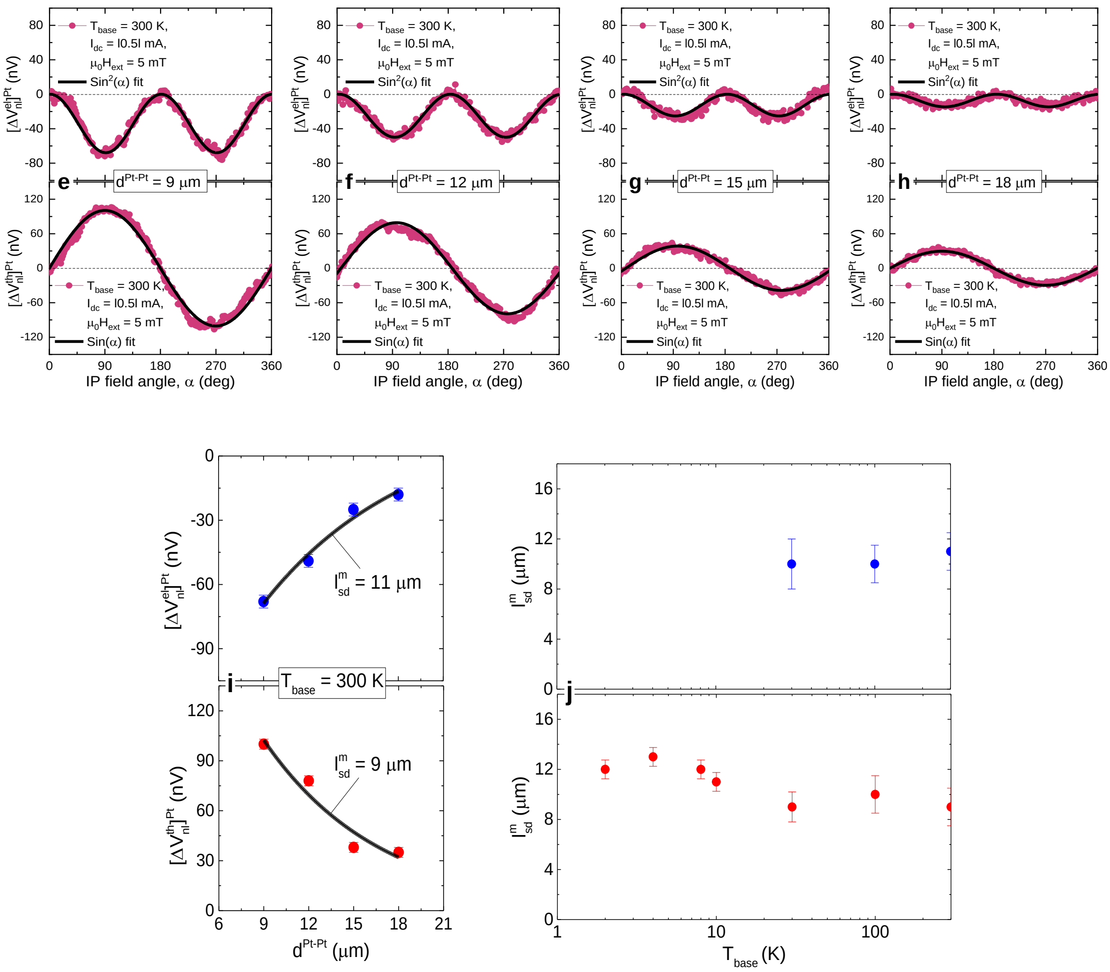

Figure S1. Non-local magnon spin-transport signals in the Pt-only reference devices. a-d, Optical micrographs of the fabricated reference devices with different d^{Pt-Pt} (9−18 μm). **e-h**, Corresponding IP field-angle α dependence of non-local voltages, ΔV_{nl}^{el} (top) and ΔV_{nl}^{th} (bottom) driven electrically and thermally, respectively, at 300 K. In these measurements, I_{dc} is fixed at |0.5| mA and the magnetic field $\mu_0 H_{\mathrm{ext}}$ at 5 mT. **i**, Summary of ΔV_{nl}^{el} (top) and ΔV_{nl}^{th} (bottom) as a function of d^{Pt-Pt}. The black solid line represents an exponential fit to estimate l_{sd}^{m}. **j**, Base temperature T_{base} evolution of the estimated l_{sd}^{m}.

Section S2. Quantification of spin currents leaking into the central Nb at room temperature.

Using the non-local magnon spin transport theory,[S4,S5,S6] we here quantify how much spin current density J_{s0}^{Pt} reaching at the YIG/Pt interface is reduced due to the presence of the central Nb. The iSHE voltages V_{iSHE}^{Pt} read in the Pt detector with and without the Al_2O_3 spin-blocking layer are, respectively, expressed as

$$V_{iSHE}^{Pt,\ with\ Al_2O_3} = \theta_{SH}^{Pt} J_{s0}^{Pt,\ with\ Al_2O_3} \left(\frac{l_{sd}^{Pt}}{t_{Pt}}\right) \tanh\left(\frac{t_{Pt}}{2l_{sd}^{Pt}}\right) \left(\frac{2e}{\hbar}\right) \rho_{Pt} l_y^{Pt}, \qquad \text{(S2a)}$$

$$V_{iSHE}^{Pt,\ no\ Al_2O_3} = \theta_{SH}^{Pt} J_{s0}^{Pt,\ no\ Al_2O_3} \left(\frac{l_{sd}^{Pt}}{t_{Pt}}\right) \tanh\left(\frac{t_{Pt}}{2l_{sd}^{Pt}}\right) \left(\frac{2e}{\hbar}\right) \rho_{Pt} l_y^{Pt}, \qquad \text{(S2b)}$$

where θ_{SH}^{Pt} (l_{sd}^{Pt}) is the spin-Hall angle (spin-diffusion length) of the Pt detector, assumed to be 0.1 (1.5 nm).[S4,S6] ρ_{Pt} is the resistivity of the Pt, which is ~28 μΩ-cm at 300 K extracted from the two-terminal Pt resistance of different thicknesses (6−10 nm). t_{Pt} (l_y^{Pt}) is the thickness (length) of the Pt. Accordingly, the reduced spin current density is

$$\Delta J_{s0}^{Pt} = J_{s0}^{Pt,\ with\ Al_2O_3} - J_{s0}^{Pt,\ no\ Al_2O_3} = \left[\frac{V_{iSHE}^{Pt,\ with\ Al_2O_3} - V_{iSHE}^{Pt,\ no\ Al_2O_3}}{\theta_{SH}^{Pt}\left(\frac{l_{sd}^{Pt}}{t_{Pt}}\right)\tanh\left(\frac{t_{Pt}}{2l_{sd}^{Pt}}\right)\left(\frac{2e}{\hbar}\right)\rho_{Pt} l_y^{Pt}}\right]. \qquad \text{(S3)}$$

Using Eq. S3 with the measured values ($\left[\Delta V_{nl}^{el}\right]^{Pt,\ no\ Al_2O_3}$, $\left[\Delta V_{nl}^{el}\right]^{Pt,\ with\ Al_2O_3}$, $\left[\Delta V_{nl}^{th}\right]^{Pt,\ no\ Al_2O_3}$, $\left[\Delta V_{nl}^{th}\right]^{Pt,\ with\ Al_2O_3}$) in Fig. 1e,f,h,i of the main text, we find Δj_{s0}^{Pt} = 2.3 A/cm^2 for electrically driven magnons and Δj_{s0}^{Pt} = 2.2 A/cm^2 for thermal driven magnons at I_{dc} = |1.0| mA (J_{dc} = |6.6| MA/cm^2). We note that the spin transfer efficiency η_s of our device ($d_x^{Pt-Pt} = 15$ μm), defined as $\eta_s = \frac{J_{s0}^{Pt}}{\theta_{SH}^{Pt} J_{dc}}$, is of the order of 10^{-5}, similar to reported from previous studies.[S4,S6]

Section S3. First-order estimate of the YIG-induced internal field at the Nb/YIG interface.

In this section, we attempt to get a first-order estimate of the YIG-induced internal field $\mu_0 H_{int}$ at the Nb/YIG interface from the measured T_c data (Fig. S2a), with *versus* without the presence of Al_2O_3 barrier between Nb and YIG films, in the framework of Ginzburg-

Landau theory:[S7,S8]

$$\mu_0 H_{int} \approx \frac{\phi_0}{2\pi[\xi(0)]^2} \cdot \left\{ \left[\frac{T_c{}^{w/\,Al_2O_3}}{T_c{}^{w/o\,Al_2O_3}} \right]^2 - 1 \right\} \qquad \text{(S4).}$$

Here k_B is Boltzmann's constant, ϕ_0 is the flux quantum ($2.07 \times 10^{-15}\, T \cdot m^2$), and $\xi(0)$ is the zero-temperature (Ginzburg-Landau) coherence length of Nb thin film (~15 nm)[S9] in the dirty limit. Since *in-plane* stray fields (from the *un-patterned/continuous* YIG) at the Nb interface do not decay significantly by the presence of the 10-nm-think Al_2O_3 barrier and their strength is in the range of 0.01 – 0.1 T,[S10,S11] we consider $\mu_0 H_{int}$ as the effective value for the exchange field h_{ex}. For the 15-nm-thick Nb layer, $T_c{}^{w/\,Al_2O_3}$ ($T_c{}^{w/0\,Al_2O_3}$) with (without) the Al_2O_3 barrier at I_{dc} = 0.0 mA is 5.50 K (4.42 K) in Fig. S2b, being as large as $\mu_0 H_{int} \approx h_{ex}$ = 1.205 T. The YIG-induced exchange spin-splitting at the Nb/YIG interface is then of 105 μeV.

It is also important to note that for the Al_2O_3-absent device in Fig. S2b, the decay of T_c with increasing I_{dc} becomes more dramatic for I_{dc} > 0.5 mA (black dashed line) than that extrapolated from direct heating of the whole device. This suggests that the strongly depressed superconductivity at a higher heating power (Fig. 3d of the main text) is likely caused by the spin-polarized QP injection/excitation into the Nb layer.

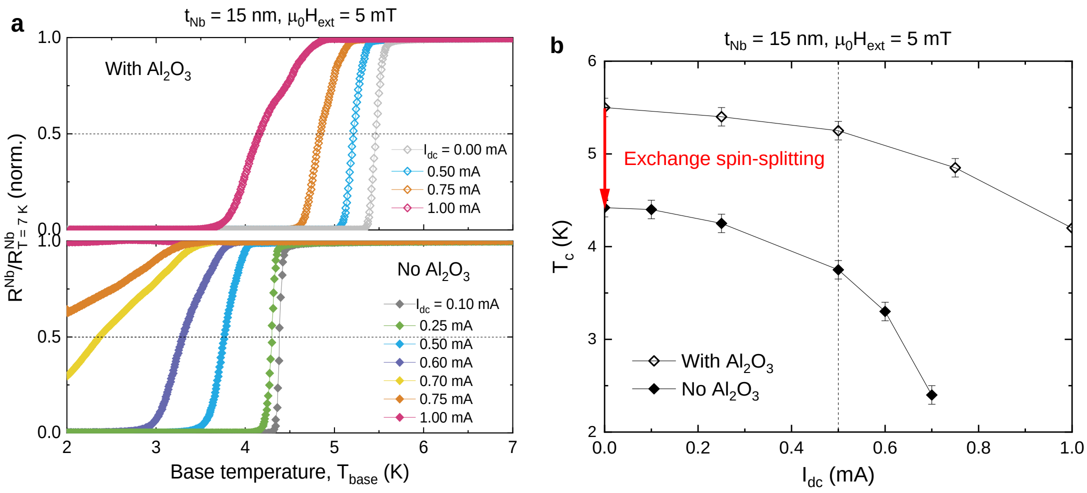

Figure S2. a, Nb resistance R^{Nb} *versus* T_{base} plots for the Al_2O_3-present (top) and Al_2O_3-

absent (bottom) devices, measured using a four-terminal current-voltage method (using leads 3,4,5,6 in Fig. 1b of the main text) while applying various I_{dc} = 0.0−1.0 mA to the Pt injector. **b**, Summary of the measured T_c as a function of I_{dc}. Note that for $I_{dc} \leq 0.5$ mA, the suppression of superconductivity by the spin-polarized QP injection/excitation is masked by the exchange spin-splitting effect (red arrow). So, the exchange spin-splitting plays a dominant role and determines the superconducting properties of the Nb layer.

Section S4. Theoretical description of the conversion efficiency of magnon spin to QP charge in the superconducting Nb.

According to the recent models[S12,S13] which explicitly take superconducting coherence peaks into account for the effective spin mixing/transfer conductance of a FMI/SC interface, the excited QP spin current density J_{s0}^{qp} from incoherent magnons is given by

$$\frac{J_{s0}^{qp}}{J_{s0}} = \frac{\int_{-\infty}^{\infty}\left[1 + \frac{\left(\Delta^{SC}\right)^2}{E(E + \Delta\mu_m)}\right][f(E) - f(E + \Delta\mu_m)]n(E)n(E + \Delta\mu_m)dE}{\Delta\mu_m}, \qquad \text{(S5)}$$

$$n(E) = \frac{|E|}{\sqrt{E^2 - \left(\Delta^{SC}\right)^2}}\theta[E^2 - (\Delta^{SC})^2], \qquad \text{(S6)}$$

where $\left[1 + \frac{\left(\Delta^{SC}\right)^2}{E(E + \Delta\mu_m)}\right]$ is the superconducting coherence factor[S14]. $\Delta^{SC}(T) = 1.76 k_B T_c \tanh\left(1.74\sqrt{1 - \frac{T}{T_c}}\right)$ is the superconducting energy gap, k_B is the Boltzmann constant and $f(E) = \frac{1}{\exp\left(\frac{E}{k_B T}\right) + 1}$ is the Fermi-Dirac (FD) distribution function. $n(E)$ is the normalized QP DOS and $\theta(E)$ is the Heaviside step function. $\Delta\mu_m$ is the magnon spin accumulation underneath the Nb detector. J_{s0} is the normal-state spin current which is directly proportional to $\Delta\mu_m$. Assuming the interface spin Seebeck coefficient S_s = 4.5 μV/K for the Pt/YIG interface[S6] and using our data set (Fig. 3,4 of the main text), we infer the J_{dc} and t_{Nb} dependence of $\Delta\mu_m$ for the calculations in Fig. 5 of the main text.

Combining Eq. S5 with Eq. S2 (but now for the Nb), we get the QP-mediated iSHE voltage[S15,S16] V_{iSHE}^{qp} in the SC detector. We have previously used this model for *metallic/conducting* Nb/Ni_8Fe_2 bilayers,[S17] but now include the superconducting coherence effect described above:

$$V_{iSHE}^{qp} = \theta_{SH}^{qp} j_{s0}^{qp} \left(\frac{l_*^{qp}}{t_{SC}}\right) \tanh\left(\frac{t_{SC}}{2l_*^{qp}}\right) \left(\frac{2e}{\hbar}\right) \rho_{SC}^* l_y \exp\left(-\frac{d_y}{\lambda_Q}\right), \quad \text{(S7a)}$$

$$V_{iSHE} = \theta_{SH} j_{s0} \left(\frac{l_{sd}}{t_{SC}}\right) \tanh\left(\frac{t_{SC}}{2l_{sd}}\right) \left(\frac{2e}{\hbar}\right) \rho_0 l_y, \quad \text{(S7b)}$$

$$\frac{V_{iSHE}^{qp}}{V_{iSHE}} = \left(\frac{\theta_{SH}^{qp}}{\theta_{SH}}\right) \left(\frac{j_{s0}^{qp}}{j_{s0}}\right) \left[\frac{l_*^{qp} \tanh\left(\frac{t_{SC}}{2l_*^{qp}}\right)}{l_{sd} \tanh\left(\frac{t_{SC}}{2l_{sd}}\right)}\right] \left[\frac{\rho_{SC}^*}{\rho_0}\right] \exp\left(-\frac{d_y}{\lambda_Q}\right), \quad \text{(S7c)}$$

$$\theta_{SH} = \theta_{SH}^{SJ} + \theta_{SH}^{SS}, \quad \text{(S8a)}$$

$$\theta_{SH}^{qp} = \theta_{SH}^{SJ} + \left[\frac{\chi_S^0(T)}{2f_0(\Delta^{SC})}\right] \cdot \theta_{SH}^{SS}, \quad \text{(S8b)}$$

$$l_{sd} = \sqrt{D\tau_{sf}}, \quad \text{(S9a)}$$

$$l_*^{qp} = \sqrt{D_S \left(\frac{1}{\tau_{sf}^{qp}} + \frac{1}{\tau_{AR}}\right)^{-1}}, \quad \text{(S9b)}$$

$$\rho_{SC}^* = \rho_{SC}^{qp} v_Q, \quad \text{(S10a)}$$

$$v_Q = \left(\frac{2\lambda_Q}{l_y}\right) \tanh\left(\frac{l_y}{2\lambda_Q}\right), \quad \text{(S10b)}$$

$$\lambda_Q = \sqrt{D_Q \tau_Q}, \quad \text{(S11)}$$

$$D_S = \left[\frac{\chi_S(T)}{2f(\Delta^{SC})}\right] D, \quad \text{(S12a)}$$

$$D_Q = \left[\frac{2f(\Delta^{SC})}{\chi_Q(T)}\right] D, \quad \text{(S12b)}$$

$$\chi_S(T) = 2\int_{\Delta^{SC}}^{\infty} \frac{E}{\sqrt{E^2 - (\Delta^{SC})^2}} \left[-\frac{\partial f(E)}{\partial E}\right] dE, \quad \text{(S13a)}$$

$$\chi_Q(T) = 2\int_{\Delta^{SC}}^{\infty} \frac{\sqrt{E^2 - (\Delta^{SC})^2}}{E} \left[-\frac{\partial f(E)}{\partial E}\right] dE, \quad \text{(S13b)}$$

where $l_y \approx l_y^{Pt} + l_{sd}^m$ is the spin-active length of the Nb detector, given approximately by the sum of the length of the Pt injector l_y^{Pt} and l_{sd}^m in our device geometry (see Fig. S5).

The postfactor $\exp\left(-\frac{d_y}{\lambda_Q}\right)$ in Eq. (S7a) represents the spatial decay of the QP charge-imbalance effect *outside* the spin-active regime of the Nb detector, where d_y is the distance between the inner edges of the QP-spin-excited Nb and the Au/Ru electrical lead (see Figs. 1b and S5b). In the following calculation, we ignore this factor as it is fundamentally linked to the QP charge-imbalance relaxation. θ_{SH} (θ_{SH}^{qp}) is the electron (QP) spin-Hall angle of the Nb in the normal (superconducting) state. We assume that the Nb spin-Hall angle is given by two extrinsic components[S15,S16] of the side jump θ_{SH}^{SJ}[S18] and the skew scattering θ_{SH}^{SS}[S19]. D_S (D_Q) is the spin (charge) diffusion coefficient of the QPs and D is the electron diffusion coefficient in the normal state. l_{sd} (τ_{sf}) is the electron spin-imbalance relaxation length (time) in the normal state. l_*^{qp} is the effective QP spin transport length considering the conversion time τ_{AR} of QPs into singlet Cooper pairs by Andreev reflection in addition to their τ_{sf}^{qp}. ρ_{SC}^* is the effective resistivity of the superconducting Nb and v_Q is the volume fraction of the QP charge imbalance.[S15,S17] $\rho_{SC}^{qp} = \frac{\rho_0}{2f_0(\Delta^{SC})}$ is the QP resistivity, ρ_0 is the residual resistivity of the Nb detector immediately above T_c and $f(\Delta^{SC}) = \frac{1}{\exp\left(\frac{\Delta^{SC}}{k_B T}\right)+1}$ is the FD distribution function at Δ^{SC}. λ_Q (τ_Q) is the QP charge-imbalance relaxation length (time). $\chi_Q(T)$ [$\chi_S(T)$] is the normalized charge (spin) susceptibility of the QPs.

To assure that j_{s0}^{qp} (Fig. 5a,b of the main text) and ρ_{SC}^* (insets of Fig. 5e,f of the main text) are governing parameters in V_{iSHE}^{qp}, we calculate how other terms $\left[\theta_{SH}^{qp},\ l_*^{qp}\tanh\left(\frac{t_{SC}}{2l_*^{qp}}\right)\right]$ in Eq. (S7c) evolve across T_c. Figure S3 shows the calculated values of $\frac{\chi_S^0(T)}{2f_0(\Delta^{SC})}$ and $l_*^{qp}\tanh\left(\frac{t_{SC}}{2l_*^{qp}}\right)$. As the superconducting transition does not influence θ_{SH}^{SJ},[S15,S16] we only consider $\theta_{SH}^{SS} \propto \frac{\chi_S^0(T)}{2f_0(\Delta^{SC})}$ [Eq. (S8b)]. We also note that if τ_{AR}

$< \tau_{sf}^{qp}$ [Eq. (S9b)], the effective transport length of QP spin is limited by the coherence length:[S20,S21] $l_*^{qp} \approx \xi_{SC}$.

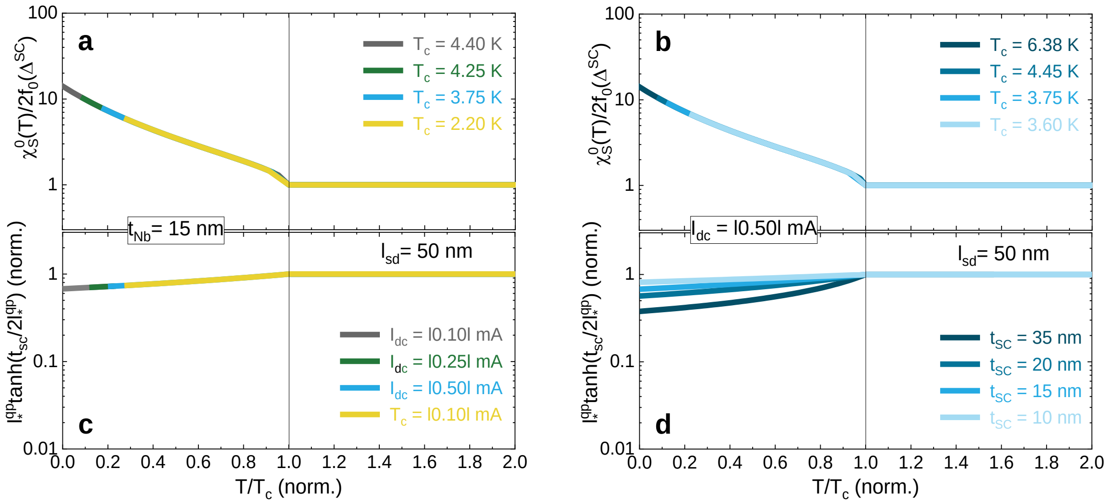

Figure S3. Model calculation. Calculated values of $\frac{\chi_S^0(T)}{2f_0(\Delta^{SC})}$ (**a**,**b**) and $l_*^{qp}\tanh\left(\frac{t_{SC}}{2l_*^{qp}}\right)$ (**c**,**d**) as a function of T/T_c. In the calculation, we use l_{sd} = 50 nm for the Nb.[S20] As can be seen in **d**, in the zero-T limit ($T/T_c \rightarrow 0$), l_*^{qp} is limited by ξ_{SC}[S20,S21] if t_{SC} is thicker.

It is evident from Fig. S3 that none of $\frac{\chi_S^0(T)}{2f_0(\Delta^{SC})}$ and $l_*^{qp}\tanh\left(\frac{t_{SC}}{2l_*^{qp}}\right)$ vary significantly in the vicinity of T_c. We therefore conclude that the giant transition-state QP iSHE observed in our system comes predominantly from a trade-off of j_{s0}^{qp} and ρ_{SC}^*, linked respectively to the superconducting coherence and the QP charge-imbalance relaxation.

Section S5. Spatially resolved measurements by varying the separation of electrical contacts on the spin-split Nb layer.

For the spatially resolved measurements presented in Fig. 6 of the main text, we prepared several independent devices on a single-piece YIG film, where only the separation distance d_s of Au/Ru electrical contacts on the 15-nm-thck Nb layer is different and it is systematically controlled by depositing a 20-nm-thick Al_2O_3 insulating layer in-between Au/Ru and Nb layers. Note that we observed d_s-independent non-local spin signals at 300 K when using the Pt detector, indicating almost similar magnon spin-transport properties in the fabricated devices (Fig. S4).

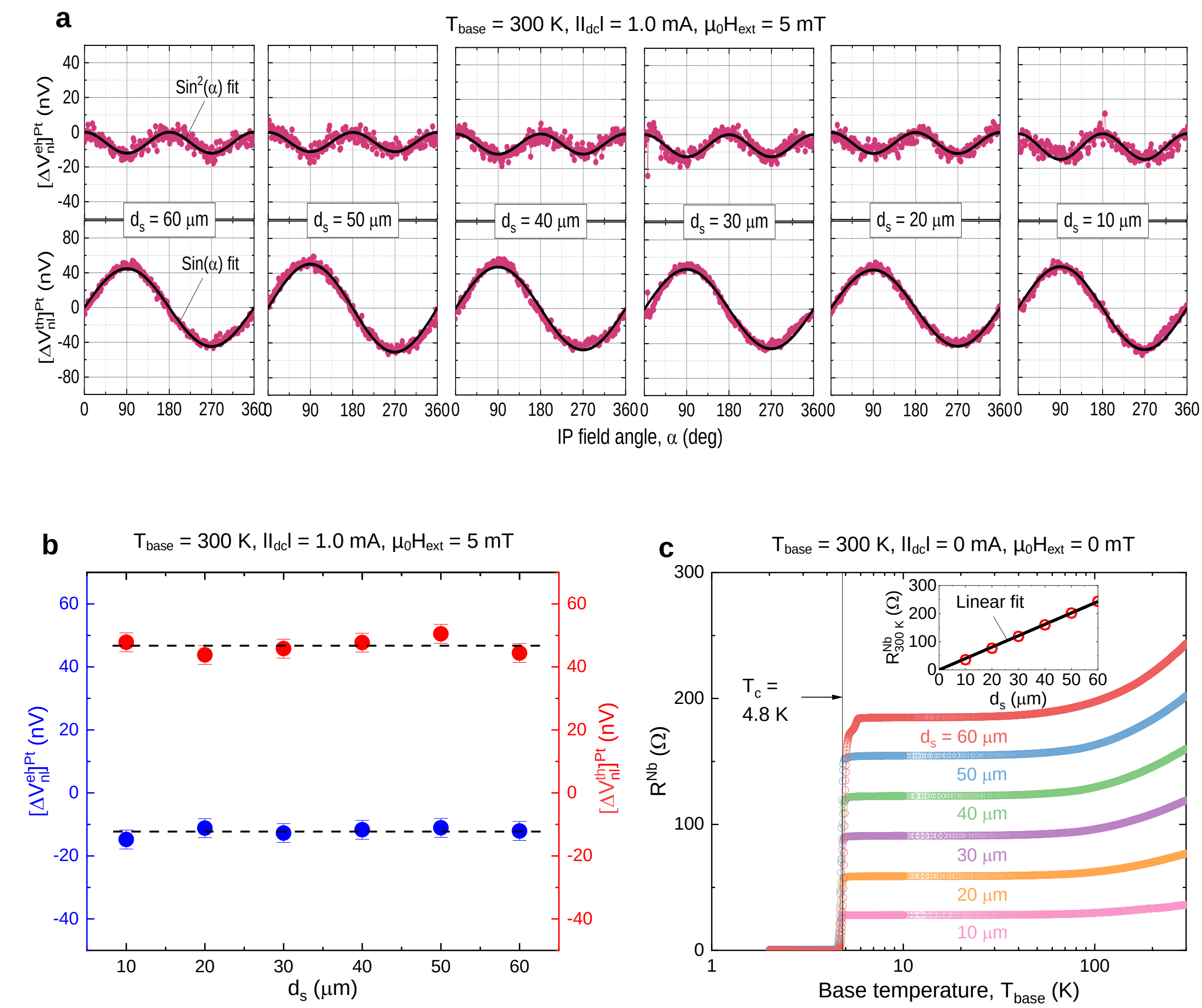

Figure S4. Non-local magnon spin-transport signals in the d_s-varying devices probed by the Pt detector. a, IP field-angle α dependence of non-local voltages, $\left[\Delta V_{nl}^{el}\right]^{Pt}$ (top) and $\left[\Delta V_{nl}^{th}\right]^{Pt}$ (bottom) driven electrically and thermally, respectively, at 300 K. In these measurements, I_{dc} is fixed at $|1.0|$ mA and the magnetic field $\mu_0 H_{ext}$ at 5 mT. **b**, Summary of $\left[\Delta V_{nl}^{el}\right]^{Pt}$ (blue) and $\left[\Delta V_{nl}^{th}\right]^{Pt}$ (red) as a function of d_s. The black dashed lines are given as guides to the eye. **c**, Overall base temperature T_{base} dependence of Nb resistance R^{Nb} for the devices with different d_s, measured using a four-terminal current-voltage method (using leads 3,4,5,6 in Fig. 6a of the main text). Note that a relatively higher T_c of the 15-nm-thick Nb layer in these devices than that of the prior device (Fig. 3d of the main text) is due to the better initial base pressure ($< 1 \times 10^{-9}$ mbar) before film deposition. The inset exhibits the d_s dependence of Nb resistance at 300K, along with a linear fit (black solid line).

As illustrated in Fig. S5, if the Au/Ru electrical contacts are placed *within* the spin-active length of the Nb detector, $d_s < l_y$, Eqs. (S7a) and (S7b) can be respectively rewritten as:

$$V_{iSHE}^{qp} = \theta_{SH}^{qp} j_{s0}^{qp} \left(\frac{l_*^{qp}}{t_{SC}}\right) \tanh\left(\frac{t_{SC}}{2l_*^{qp}}\right) \left(\frac{2e}{\hbar}\right) \rho_{SC}^* d_s \exp\left[-\frac{(l_y - d_s)}{\lambda_Q}\right], \qquad \text{(S14a)}$$

$$V_{iSHE} = \theta_{SH} j_{s0} \left(\frac{l_{sd}}{t_{SC}}\right) \tanh\left(\frac{t_{SC}}{2l_{sd}}\right) \left(\frac{2e}{\hbar}\right) \rho_0 d_s, \qquad \text{(S14b)}$$

Here, $\exp\left[-\frac{(l_y - d_s)}{\lambda_Q}\right]$ describes the characteristic spatial dependence of QP charge-imbalance relaxation effect[S16] *inside* the spin-active regime of the Nb detector.

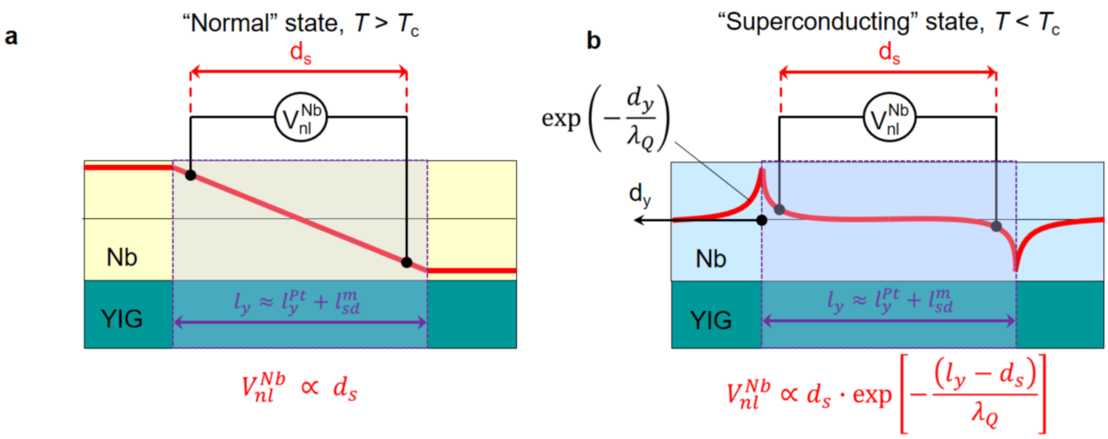

Figure S5. Transverse spatial profile of the iSHE voltage $V_{iSHE}^{(qp)}$ induced by non-local magnon spin-transport in Nb/YIG layers above (a) and below (b) the

superconducting transition T_c of Nb. In b, $\exp\left[-\frac{(l_y - d_s)}{\lambda_Q}\right]$ describes the characteristic spatial dependence of QP charge-imbalance relaxation effect[S16] *inside* the spin-active regime of the Nb layer, where d_s is the separation distance of electrical contacts on the Nb and λ_Q is the QP charge-imbalance relaxation length. The wine dashed line represents the spin-active regime that is given approximately by the sum of the length of the Pt injector l_y^{Pt} and the magnon spin-diffusion length l_{sd}^{m} in our device geometry. Note that if the electrical contacts are placed *outside* the spin-active regime, $V_{iSHE}^{qp} \propto \exp\left(\frac{-d_y}{\lambda_Q}\right)$.[S16,S17,S22] Here, d_y is the distance between the inner edges of the QP-spin-excited Nb and the electrical contact.

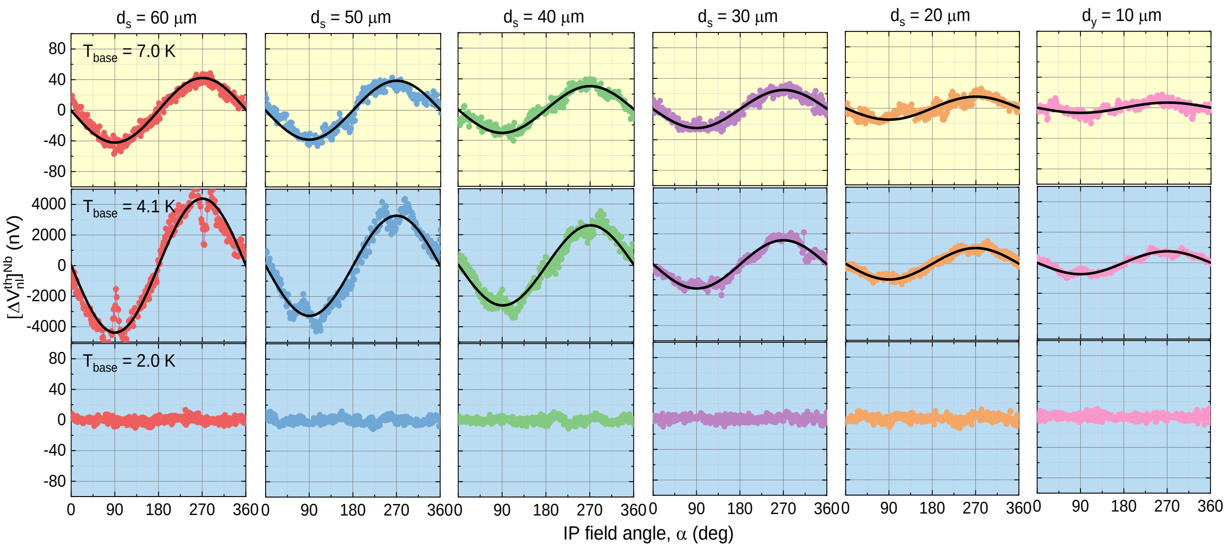

Figure S6. Non-local magnon spin-transport signals in the d_s-varying devices measured by the Nb detector. Typical examples of thermally driven non-local voltages $\left[\Delta V_{nl}^{th}(\alpha)\right]^{Nb}$ as a function of IP field angle α for the devices with different d_s, taken above (top), immediately below (middle), and far below (bottom) T_c of the Nb layer, from which the data presented in Fig. 6b of the main text was extracted. The black solid lines are $\sin(\alpha)$ fits. In these measurements, I_{dc} is fixed at $|0.5|$ mA and the magnetic field $\mu_0 H_{ext}$ at 5 mT.

References

(S1) Shan, J.; Cornelissen, L. J.; Liu, J.; Ben Youssef, J.; Liang, L.; van Wees, B. J. Criteria for Accurate Determination of the Magnon Relaxation Length from the Nonlocal Spin Seebeck Effect. *Phys. Rev. B* **2017**, *96*, 184427.

(S2) Cornelissen, L. J.; Liu, J.; Duine, R. A.; Ben Youssef, J.; van Wees, B. J. Long-Distance Transport of Magnon Spin Information in a Magnetic Insulator at Room Temperature. *Nat. Phys.* **2015**, *11*, 1022–1026.

(S3) Cornelissen, L. J.; Shan, J.; van Wees, B. J. Temperature Dependence of the Magnon Spin Diffusion Length and Magnon Spin Conductivity in the Magnetic Insulator Yttrium Iron Garnet. *Phys. Rev. B* **2016**, *94*, 180402(R).

(S4) Cornelissen, L. J.; Peters, K. J. H.; Bauer, G. E. W.; Duine, R. A.; van Wees, B. J. Magnon Spin Transport Driven by the Magnon Chemical Potential in a Magnetic Insulator. *Phys. Rev. B* **2016**, *94*, 014412.

(S5) Bender, S. A.; Duine, R. A.; Tserkovnyak, Y. Electronic Pumping of Quasi Equilibrium Bose-Einstein-Condensed Magnons. *Phys. Rev. Lett.* **2012**, *108*, 246601.

(S6) Shan, J.; Cornelissen, L. J.; Vlietstra, N.; Youssef, J. B.; Kuschel, T.; Duine, R. A.; van Wees, B. J. Influence of Yttrium Iron Garnet Thickness and Heater Opacity on the Nonlocal Transport of Electrically and Thermally Excited Magnons. *Phy. Rev. B* **2016**, *94*, 174437.

(S7) Landau, L. D.; Ginzburg, V. L. On the Theory of Superconductivity. *Zh. Eksp. Teor. Fiz.* **1950**, *20*, 1064–1082.

(S8) Banerjee, N.; Ouassou, J. A.; Zhu, Y.; Stelmashenko, N. A.; Linder, J.; Blamire, M. G. Controlling the Superconducting Transition by Spin-Orbit Coupling. *Phys. Rev. B* **2018**, *97*, 184521.

(S9) Gu, J. Y.; Caballero, J. A.; Slater, R. D.; Loloee, R.; Pratt, W. P. Direct Measurement of Quasiparticle Evanescent Waves in a Dirty Superconductor. *Phys. Rev. B* **2002**, *66*, 140507(R).

(S10) Nogaret, A. Electron Dynamics in Inhomogeneous Magnetic Fields. *J. Phys.: Condens. Matter* **2010**, *22*, 253201.

(S11) Dash, S. P.; Sharma, S.; Le Breton, J. C.; Peiro, J.; Jaffrès, H.; George, J.-M.; Lemaître, A.; Jansen, R. Spin Precession and Inverted Hanle Effect in a Semiconductor near a Finite-Roughness Ferromagnetic Interface. *Phys. Rev. B* **2011**, *84*, 054410.

(S12) Inoue, M.; Ichioka, M.; Adachi, H. Spin Pumping into Superconductors: A New Probe of Spin Dynamics in a Superconducting Thin Film. *Phys. Rev. B* **2017**, *96*, 024414.

(S13) Kato, T.; Ohnuma, Y.; Matsuo, M.; Rech, J.; Jonckheere, T.; Martin, T. Microscopic Theory of Spin Transport at the Interface between a Superconductor and a Ferromagnetic Insulator. *Phys. Rev. B* **2019**, *99*, 144411.

(S14) Klein, O.; Nicol, E. J.; Holczer, K.; Gru¨ner, G. Conductivity Coherence Factors in the Conventional Superconductors Nb and Pb. *Phys. Rev. B* **1994**, *50*, 6307.

(S15) Takahashi, S.; Maekawa, S. Hall Effect Induced by a Spin-Polarized Current in Superconductors, *Phys. Rev. Lett.* **2002**, *88*, 116601.

(S16) Takahashi, S.; Maekawa, S. Spin Hall Effect in Superconductors. *Jpn. J. Appl. Phys.* **2012**, *51*, 010110.

(S17) Jeon, K.-R.; Ciccarelli, C.; Kurebayashi, H.; Wunderlich, J.; Cohen, L. F.; Komori, S.; Robinson, J. W. A.; Blamire, M. G. Spin-Pumping-Induced Inverse Spin-Hall Effect in Nb/$Ni_{80}Fe_{20}$ Bilayers and Its Strong Decay across the Superconducting Transition Temperature. *Phys. Rev. Applied* **2018**, *10*, 014029.

(S18) Berger, L. Side-Jump Mechanism for the Hall Effect of Ferromagnets. *Phys. Rev. B* **1970**, *2*, 4559.

(S19) Smit, J. The Spontaneous Hall Effect in Ferromagnetics I, *Physica* **1955**, *21*, 877(1955); Smit, J. The Spontaneous Hall Effect in Ferromagnetics II, *Physica* **1958**, *24*, 39.

(S20) Gu, J. Y.; Caballero, J. A.; Slater, R. D.; Loloee, R.; Pratt, W. P. Direct Measurement of Quasiparticle Evanescent Waves in a Dirty Superconductor. *Phys. Rev. B* **2002**, *66*, 140507.

(S21) Yamashita, T.; Takahashi, S.; Imamura, H.; Maekawa, S. Spin Transport and Relaxation in Superconductors. *Phys. Rev. B* **2002**, *65*, 172509.

(S22) Wakamura, T.; Akaike, H.; Omori, Y.; Niimi, Y.; Takahashi, S.; Fujimaki, A.; Maekawa, A.; Otani, Y. Quasiparticle-Mediated Spin Hall Effect in a Superconductor. *Nat. Mater.* **2015**, *14*, 675–678.